# The Nanotech France 2023 International Conference

# June 28 to 30 2023
# Conference Proceedings

# Modular Infrared Heater with Nanofluid Thermal Accumulation Collector - Unsteady Entropy Analysis

Fikret Alic

Department of Thermal and Fluid Technique, Faculty of Mechanical Engineering, University of Tuzla, Tuzla, Bosnia and Herzegovina, fikret.alic@untz.ba

## Abstract

The heating of a body (heat target, HT) by thermal radiation is often accompanied by heat losses, caused by the scattering of thermal rays and by not hitting its surface. These losses occur in infrared heating of different rooms. The heat source, i.e. modular infrared heater, can change the output intensity of thermal radiation within various wavelength intervals. Although there are different combinations of modular infrared heaters with variations in power, and geometric position in relation to HT, in this paper one characteristic combination, is analyzed. By setting the HT on the surface of the nanofluid collector with nano-enhanced phase change material (NePCM), it enables the increase in the overall efficiency of this heating process. The nanofluid collector consists of a complex pipe element through which the nanofluid flows, and a collector inside which the thermal-accumulating NePCM is placed. According to their characteristics, infrared thermal rays heat only HT, while the heating of the ambient air through which they pass is negligible. Based on this fact, the accumulated heat inside the NePCM can be used for convective heating of the ambient air around the HT surface. This process reduces the convective heat dissipation from HT to the ambient air and increases the efficiency of the modular infrared heat source. Furthermore, the accumulated heat inside the NePCM can be used for various technical applications. In this study, a mathematical model of the unsteady thermal entropy generation of the described heating system is established. By finding the unsteady thermal entropy, the next process of minimizing thermal irreversibility and maximizing the energy efficiency of the analyzed system is enabled. The volume fraction ratio of $Al_2O_3$ nanoparticles varies within the base fluid (water). Furthermore, the temperature of the infrared heaters varies as well as the volume fraction ratio of $Al_2O_3$ within the NePCM.

**Keywords:** infrared heater, thermal radiation, nanofluid, nano-enhanced phase change material, accumulation collector, unsteady entropy, unsteady energy efficiency

## 1. Introduction

Heat transfer by short-wave infrared thermal radiation causes heating of the heating target, but not of the air through which the thermal rays pass. On the other hand, long-wave thermal radiation is not characterized by the absence of air heating and its circulation caused by natural convection. The frequency of short-wave infrared radiation passes through the air and does not cause its molecular vibrations and rotations. Sources of short-wave infrared radiation can be different heating sources of high temperatures.

Temperature and wavelength are interconnected, so high temperature directly implies the small wavelength and high frequency. Therefore, only heat exchange by thermal radiation at short wavelengths is established between the heating source and the heat target. The values of the efficiency of heating by thermal radiation of the heating target depend both on their temperatures and emissivity, as well as on their mutual spatial position. Many experimental and mathematical analyzes describe the efficiency of the net heat exchange by radiation between the heating source and the heat target. Any heating, cooling, or any change in the phase of a material causes a change in the total entropy of the system. The entropy generation can include both thermal and hydraulic entropy, depending on whether there are hydraulic losses caused by fluid movement. As follows, many studies based the methodology on the analysis of the total entropy of the system, second law analysis, which includes radiative heat transfer and radiative entropy generation, referenced from [1] to [4]. A change in thermal and hydraulic entropy also occurs by changing the volume fraction ratio of nanoparticles in nanofluids. By adding nanoparticles to the base fluid and their dispersion, some of the physical properties of the nanofluid are improved, and it directly affects the intensification of heat exchange. As a result of the above, there is a change in thermal entropy. Nanoparticles inside affect the frictional properties of the nanofluid, i.e. its hydraulic entropy. Many researchers analyze and study the influence of the type, size and volume fraction ratio of nanoparticles on heat transfer, hydraulic properties, or the total entropy of the system, referenced from [5] to [7]. Phase change material (PCM) is widely used in various processes of exchange and

accumulation of thermal energy. By adding and dispersing nanoparticles inside PCM, some of its thermal properties are improved, while such a material is called Nano enhanced phase change material (NePCM). Some studies compare the effect of nanoparticles on the thermal irreversibility of the finally formed NePCM, based from [8] to [10]. In the context of the research polygon and methodology in this work, the characteristic of thermal heating of the heating target is the scattering of thermal rays from the heat source that do not hit the heat target but are absorbed in the environment of the heat target, Figure 1.
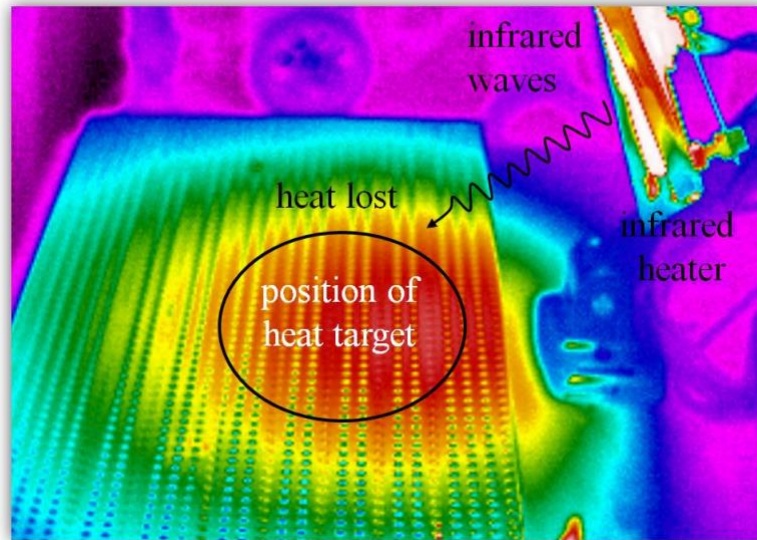


**Fig. 1**: The scattering of thermal radiation reduces the efficiency of the heat source.

This part of the thermal energy from the heat source is irreversibly lost and the heating efficiency decreases. It is this feature of short-wave heating by thermal radiation of the heating target that initiated the idea of absorbing that part of the thermal radiation that does not hit the heating target and its subsequent use. In this sense, a thermal collector was designed on which the heating target is placed. Nano enhanced phase change material (NePCM) is placed inside the thermal collector, which has the ability to change phase and accumulate thermal energy. NePCM will change phase from solid to liquid after accumulating heat. Subsequent removal of heat from the liquefied NePCM causes it to solidify again.

## 2. Methodology

### 2.1. Heat balance

Between the heat source of variable power and the heat target (HT), heat exchange is established by thermal radiation. The heat source simultaneously heats the heat target and the NePCM, with short-wave infrared radiation, while the heating of the surrounding air is neglected, Figure 2. According to Figure 2, the heat source and heat target are placed in parallel, so the heat exchange in the conditions shown can be represented by the following balance, Eq. (1).
This balance does not take into account the negligible heating of the surrounding air by the heat target, and analyzes a short heating interval. The change in the temperature of the heat target over time depends on the difference in temperature of the heat source and the heat target, their emissivity and their mutual geometric position.
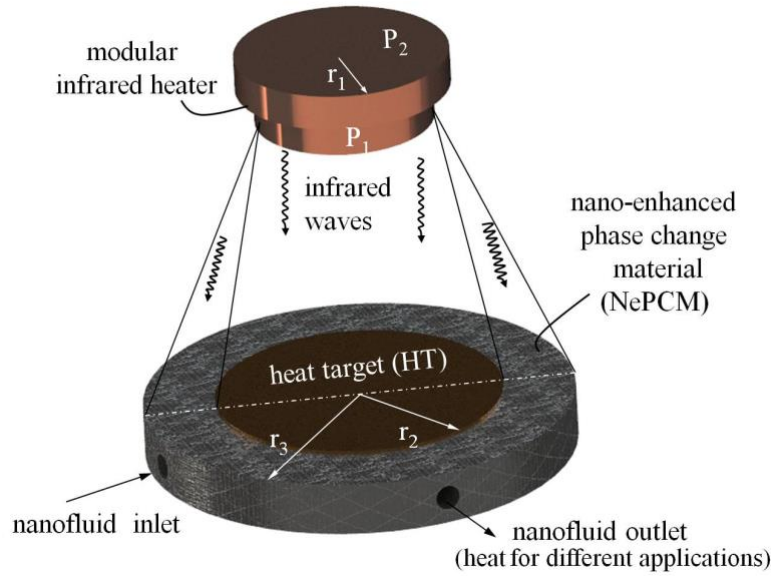
**Fig. 2**: The heating of the heat target by thermal radiation is accompanied by the dissipation of thermal energy.

$$\rho_{ht} c_{ht} V_{ht} \frac{dT_{ht}}{d\tau} = \frac{\sigma(T_H^4 - T_{ht}^4)}{\frac{1 - \varepsilon_H}{\varepsilon_H A_H} + \frac{1}{F_{H-ht} A_H} + \frac{1 - \varepsilon_{ht}}{\varepsilon_{ht} A_{ht}}} \tag{1}$$

and after separation of variables and integration

$$\int_{T_{ht.o}}^{T_{ht}} \frac{dT_{ht}}{T_H^4 - T_{ht}^4} = \frac{\sigma}{\rho_{ht} c_{ht} V_{ht} \left( \frac{1 - \varepsilon_H}{\varepsilon_H A_H} + \frac{1}{F_{H-ht} A_H} + \frac{1 - \varepsilon_{ht}}{\varepsilon_{ht} A_{ht}} \right)} \tau \tag{2}$$

the temperature change of the heat target over time is obtained, Eq. (3),

$$-\frac{1}{4} \ln \left( \frac{T_H + T_{ht}}{T_H + T_{ht.o}} \right) + \frac{1}{4} \ln \left( \frac{T_H - T_{ht}}{T_H - T_{ht.o}} \right) - \frac{1}{2} \left[ \arctan \left( \frac{T_{ht}}{T_H} \right) - \arctan \left( \frac{T_{ht.o}}{T_H} \right) \right]$$
$$= \frac{\sigma}{\rho_{ht} c_{ht} V_{ht} \left( \frac{1 - \varepsilon_H}{\varepsilon_H A_H} + \frac{1}{F_{H-ht} A_H} + \frac{1 - \varepsilon_{ht}}{\varepsilon_{ht} A_{ht}} \right)} \tau \tag{3}$$

where $T_{ht.o}$ is the initial temperature of the heat target, $\varepsilon_H$ $A_H$ and $\varepsilon_{ht}$ , $A_{ht}$ emission coefficients of the heat source and heat target and their surfaces, respectively. Visible factor between two parallel surfaces, Figure 2, heat source and heat target, can be determined from

$$F_{H-hT} = \frac{1}{2} \left\{ 1 + \frac{1 + \left( \frac{r_2}{h} \right)^2}{\left( \frac{r_1}{h} \right)^2} - \left[ \left[ 1 + \frac{1 + \left( \frac{r_2}{h} \right)^2}{\left( \frac{r_1}{h} \right)^2} \right]^2 - 4 \left( \frac{D_{hT}}{D_H} \right)^2 \right]^{0.5} \right\} \tag{4}$$

where $h$ is the shortest vertical distance between the heat source and the heat target. By simplifying Eq. (3), by introducing that the temperature $T_{hT} \ll T_H$, an expression for calculating the heat target temperature is obtained

$$-\frac{1}{4}\ln\left(1 + \frac{T_{ht}}{T_H}\right) + \frac{1}{4}\ln\left(1 - \frac{T_{ht}}{T_H}\right) - \frac{1}{2}\arctan\left(\frac{T_{ht}}{T_H}\right) \approx -\frac{1}{4}\frac{T_{ht}}{T_H} - \frac{1}{4}\frac{T_{ht}}{T_H} - \frac{1}{2}\frac{T_{ht}}{T_H}$$

$$= -\frac{T_{ht}}{T_H}$$

$$= \frac{\sigma}{\rho_{ht}c_{ht}V_{ht}\left(\frac{1-\varepsilon_H}{\varepsilon_H A_H} + \frac{1}{F_{H-ht}A_H} + \frac{1-\varepsilon_{ht}}{\varepsilon_{ht}A_{ht}}\right)}\tau - \frac{1}{4}\ln(T_H + T_{ht.o}) \qquad (5)$$

$$+ \frac{1}{4}\ln(T_H - T_{ht.o}) - \frac{1}{2}\arctan\left(\frac{T_{ht.o}}{T_H}\right)$$

$$T_{ht} = T_H\frac{1}{4}\ln(T_H + T_{ht.o}) - \frac{\sigma T_H}{\rho_{ht}c_{ht}V_{ht}\left(\frac{1-\varepsilon_H}{\varepsilon_H A_H} + \frac{1}{F_{H-ht}A_H} + \frac{1-\varepsilon_{ht}}{\varepsilon_{ht}A_{ht}}\right)}\tau \qquad (6)$$

$$- T_H\frac{1}{4}\ln(T_H - T_{ht.o}) + T_H\frac{1}{2}\arctan\left(\frac{T_{ht.o}}{T_H}\right)$$

A part of the thermal radiation sent from the heat source does not hit the target but the collector surface $A_c$. For the above reason, a part of the energy is accumulated inside the collector, which can be used indirectly. The collector temperature change is on a similar balance as described by Eq. (1),

$$\int_{T_{pcm.o}}^{T_{pcm}}\frac{dT_{pcm}}{T_H^4 - T_{pcm}^4} = \frac{\sigma}{\rho_{pcm}c_{pcm}V_{pcm}\left(\frac{1-\varepsilon_H}{\varepsilon_H A_H} + \frac{1}{F_{H-c}A_H} + \frac{1-\varepsilon_c}{\varepsilon_c A_c}\right)}\tau \qquad (7)$$

where it is obtained from

$$-\frac{1}{4}\ln\left(\frac{T_{pcm} + T_H}{T_{pcm.o} + T_H}\right) + \frac{1}{4}\ln\left(\frac{T_H - T_{pcm}}{T_H - T_{pcm.o}}\right) - \frac{1}{2}\left[\arctan\left(\frac{T_{pcm}}{T_H}\right) - \arctan\left(\frac{T_{pcm.o}}{T_H}\right)\right]$$

$$= \frac{\sigma}{\rho_{pcm}c_{pcm}V_{pcm}\left(\frac{1-\varepsilon_H}{\varepsilon_H A_H} + \frac{1}{F_{H-c}A_H} + \frac{1-\varepsilon_c}{\varepsilon_c A_c}\right)}\tau \qquad (8)$$

where in this case the visibility factor between the surface $A_H$ and $A_C$ is calculated from the following expression.

$$F_{H-c} = \frac{1}{2}\left\{\left(\frac{r_3}{r_1}\right)_3^2 - \left(\frac{r_2}{r_1}\right)_2^2 - \left[\left(1 + \left(\frac{r_3}{r_1}\right)_3^2 + \left(\frac{h}{r_1}\right)_1^2\right)^2 - 4\left(\frac{r_3}{r_1}\right)_3^2\right]^{0.5}\right. \qquad (9)$$

$$\left. + \left[\left(1 + \left(\frac{r_2}{r_1}\right)_2^2 + \left(\frac{h}{r_1}\right)_1^2\right)^2 - 4\left(\frac{r_2}{r_1}\right)_2^2\right]^{0.5}\right\}$$

$$T_{pcm} = T_H\frac{1}{4}\ln(T_H + T_{pcm.o}) - \frac{\sigma T_H}{\rho_{pcm}c_{pcm}V_{pcm}\left(\frac{1-\varepsilon_H}{\varepsilon_H A_H} + \frac{1}{F_{H-c}A_H} + \frac{1-\varepsilon_c}{\varepsilon_c A_c}\right)}\tau$$

$$- T_H\frac{1}{4}\ln(T_H - T_{pcm.o}) + T_H\frac{1}{2}\arctan\left(\frac{T_{pcm.o}}{T_H}\right) \qquad (10)$$

The collector material is a nanofluid collector with NePCM, so the change in physical properties of NePCM was adopted.

$$\rho_{pcm} = \frac{\varrho_p V_p + \varrho_{pcm.o} V_{pcm.o}}{V_p + V_{pcm.o}} = \varphi \rho_p + (1 - \varphi)\rho_{pcm.o} \tag{11}$$

$$c_{pcm} = \frac{\rho_p c_p \varphi + (1 - \varphi)\rho_{pcm.o} c_{pcm.o}}{\rho_p \varphi + (1 - \varphi)\rho_{pcm.o}} \tag{12}$$

In the previous equations, $\rho_{pcm.o}$ and $c_{pcm.o}$ represent the density and specific heat capacity of the basic PCM without added nanoparticles, while $\varphi$ is the volume fraction ratio of nanoparticles. After adding nanoparticles, the specified physical properties for the NePCM are marked with $\rho_{pcm}$ and $c_{pcm}$.

## 2.2. Entropy generation

Thermally generated entropy in this analysis includes the heat source, heat target and collector in which the nano-enhanced phase change material is placed. The thermal entropy of the heat source is represented by Eq. (13), is negative and takes into account heat exchange by radiation between the heat source and the heat target, and the collector. The temperature of the heat source ($T_H$) was considered constant, and that the complete thermal energy is directed towards the heat target and the collector.

$$\begin{aligned}
\left(S_{gen.T}\right)_{HS} &= -\frac{Q_H}{T_H} = -\frac{Q_{H-ht}}{T_H} - \frac{Q_{H-c}}{T_H} \\
&= -\frac{\sigma A_H F_{H-hp}(T_H^4 - T_{ht}^4)}{T_H} - \frac{\sigma A_H F_{H-c}(T_H^4 - T_c^4)}{T_H}
\end{aligned} \tag{13}$$

The heat energy receiver, heat target ($T_{ht}$) and collector have a positive value of transient thermal entropy, since their temperature increases over time, equation (14). Since the wall of the collector housing is thin, it is considered that the temperature of the collector is $T_c = T_{pcm}$.

$$\left(S_{gen.T}\right)_{ht,pcm} = \frac{d}{d\tau} m_{ht} c_{ht} ln(T_{ht}) + \frac{d}{d\tau} m_{pcm} c_{pcm} ln(T_{pcm}) \tag{14}$$

## 2.2. Results

The influence of the variation of the volume fraction ratio of $Al_2O_3$ nanoparticles on the transient value of thermal entropy, during the heating of the heat target for 150s, is shown in Figure 3. Two various materials, gypsum and aluminium represent the heat target which are alternately heated by a short-wave infrared source at a constant temperature of 950K. The surface of polished aluminium and gypsum has an emissivity of 0.2 and 0.8, respectively. Other characteristic geometric parameters and physical sizes of these two heat targets are shown in Table 1 and Figure 3. Volume fraction ratio of $Al_2O_3$ within NePCM varied in the amounts of 2, 6, and 9%.

Table 1: Physical properties of nanoparticles, base liquid, and characteristic geometrical parameters.

| Properties of nanoparticles ($Al_2O_3$) | | Properties of base liquid - sodium acetate trihydrate | | Geometric parameters | | | |
|---|---|---|---|---|---|---|---|
| $\rho_p$ [kgm$^{-3}$] | $c_p$ [Jkg$^{-1}$K$^{-1}$] | $\rho_{bf}$ [kgm$^{-3}$] | $c_{bf}$ [Jkg$^{-1}$K$^{-1}$] | $h$ [m] | $r_1$ [m] | $r_2$ [m] | $r_3$ [m] |
| 3970 | 756 | 1450 | 3100 | 0.25 | 0.06 | 0.1 | 0.15 |

At the established values and limitations, the total thermal entropy when using gypsum as a heat target is higher than that of aluminium and its value decreases rapidly over time. The effect of increasing the volume fraction ratio of $Al_2O_3$ within NePCM slightly increases the total thermal entropy only during longer heating of the heat target, after 100s.
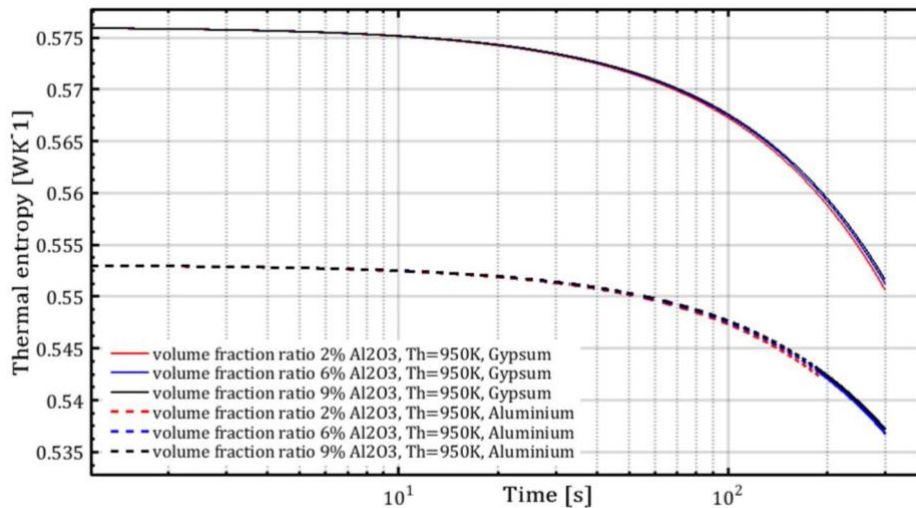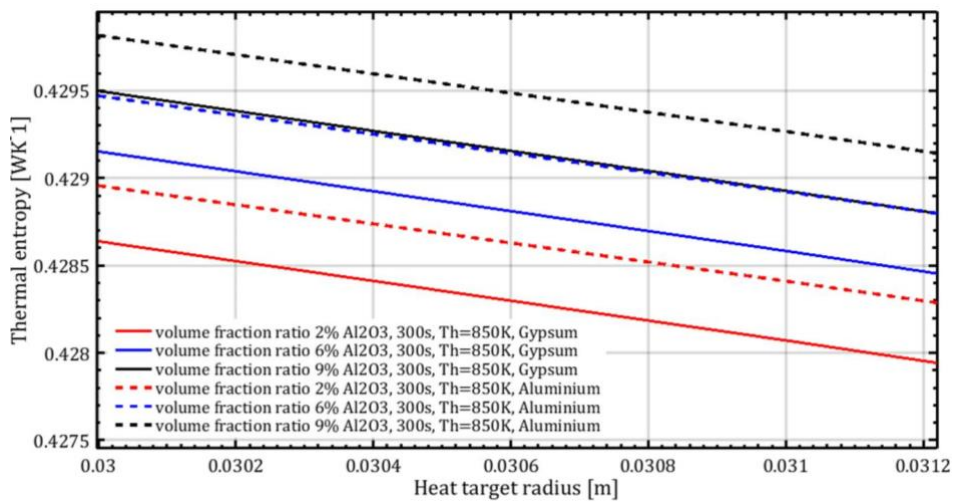
**Fig. 3**: Total thermal entropy, at a constant temperature of the heating source.

When the temperature of the heating source varies from 750, 850, and 950K and the volume fraction ratio of $Al_2O_3$ is constant in the amount of 6%, the total thermal entropy is significantly different in value, Figure 4, than it was in the previous case.
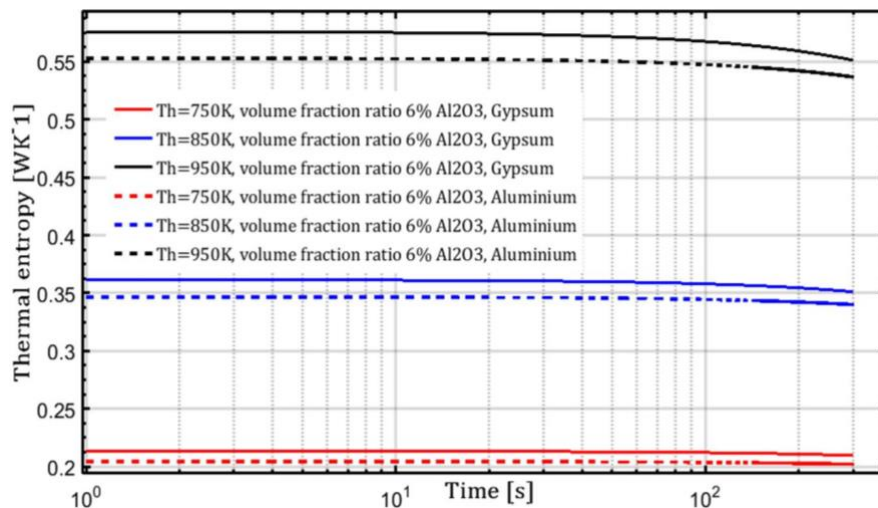


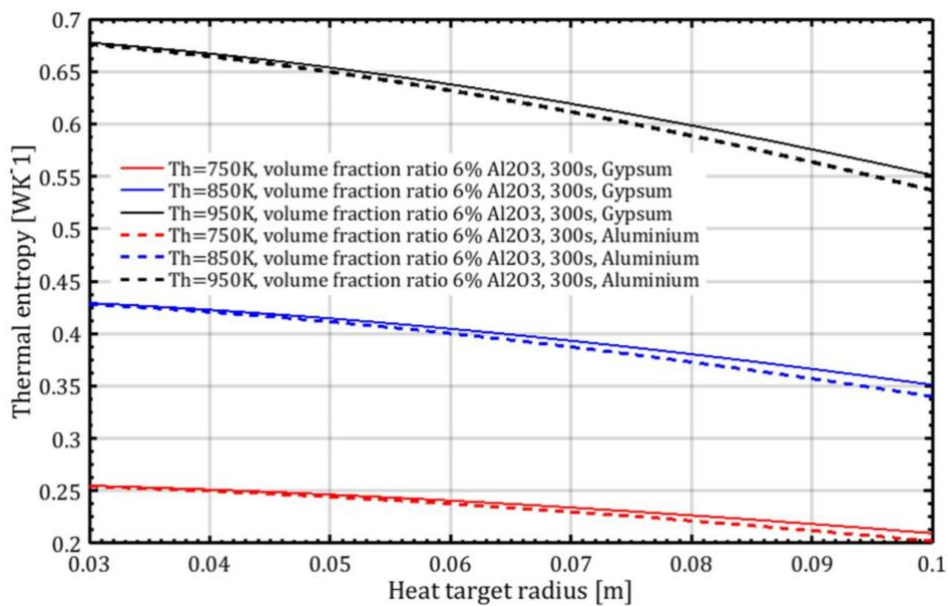**Fig. 4**: Total thermal entropy-temperature of the heating source varies.

The effect of increasing the temperature of the heating source of 950K on the total thermal entropy has the highest values when using gypsum as a heat target. Smaller values are obtained for the case of using aluminium. Significantly lower values of thermal entropy were recorded at the lowest temperature of the heating source of 750K, Figure 4. The values of the total thermal entropy are almost constant throughout the entire time interval. Increasing the radius of the heat target at a constant temperature of the heating source of 850K affects the linear decrease of the total thermal entropy of both analyzed materials, Figure 5. Volume fraction ratio in the maximum amount of 9% $Al_2O_3$ within NePCM has the highest value of thermal entropy in both analyzed materials. Quantitatively small differences in thermal entropy values occur when aluminium is used as a heat target.

**Fig. 5**: The effect of changing the radius of the heat target on the total thermal entropy.

The cross-change of the heat target radius and the temperature of the heating source, while maintaining the constant volume fraction ratio of $Al_2O_3$ of 6%, is shown in Figure 6. At the minimum temperature of the heating source of 750K, the thermal entropy values are the lowest for both tested materials, with a slightly higher value for gypsum. By increasing the heat target radius, the total thermal entropy decreases approximately linearly, regardless of the value of the temperature of the heat source and the type of material of the heat target.



**Fig. 6**: Cross change of the radius of the heat target and the temperature of the heating source.

### 3. Conclusion

The analytical modelling of the unsteady thermal entropy analysis of the heat source, heat target and NePCM collector was analysed in this paper. The heat transfer from the source to the heat target and NePCM is established by short-wave radiation, while the heating of the ambient air is neglected. The geometrical position of the heat target and the NePCM material causes their different visibility factor. The heater temperature and volume fraction ratio of $Al_2O_3$ nanoparticles vary within the base fluid (distilled water). The established analytical model of the thermal entropy can be the basis for various processes.

Total thermal entropy decreases during heating, with the main heat transfer being achieved by thermal radiation.

- Increasing the temperature of the heat source increases the total thermal entropy many times over.

- Increasing the volume fraction ratio within the phase change material to a lesser extent increases the total thermal entropy.

Otherwise, the obtained analytical methodology in this paper can represent the basis for the optimization of the process with controlled infrared heating and heat accumulation within NePCM.

## Acknowledgements

## References

1. D. Makhanlall et al., "SLA (Second-law analysis) of transient radiative transfer processes," *Energy*, vol. 35, no.12, pp. 5151-5160, 2010.
2. S.E. Wright, et al., "On the entropy of radiative heat transfer in engineering thermodynamics." *International Journal of Engineering Science*, vol. 39, 15, pp. 1691-1706, 2001.
3. Vedat S. A., "Radiative entropy production-lost heat into entropy," *International Journal of Heat and Mass Transfer*, vol. 30, no.10, pp. 2115-2123, 1987.
4. Asadollah B., Ali S. and Hossein A., "Analysis of spectral radiative entropy generation in a non-gray planar participating medium at radiative equilibrium with two different boundary conditions," *International Journal of Thermal Sciences*, vol.146, 106073, 2019.
5. Alic, F., "Entransy Dissipation Analysis and New Irreversibility Dimension Ratio of Nanofluid Flow Through Adaptive Heating Elements," *Energies*., vol.13, no.114, 2020.
6. Omid M., et al., "A review of entropy generation in nanofluid flow," *International Journal of Heat and Mass Transfer*, vol. 65, pp. 514-532, 2013.
7. Alic, F., "The non-dimensional analysis of nanofluid irreversibility within novel adaptive process electric heaters," *Applied Thermal Engineering*., vol.152, pp. 13-23, 2019.
8. Syeda, L.T, et al., "Nanoparticles enhanced phase change materials (NePCMs)-A recent review," *Applied Thermal Engineering*, vol. 176, 115305, 2020.
9. Bellecci, C. and Conti, M., "Phase change energy storage: entropy production, irreversibility and second law efficiency," *Solar energy*., vol.53, pp. 163-170, 1994b.
10. Amin S., et al., "Entropy generation characteristics of phase change material in a variable wavy walled triplex tube latent heat storage unit for battery thermal management system," *Journal of Energy Storage*, vol. 51, 104374, 2022.

# MoS$_2$ nanowires *in-situ* sputtered with Molybdenum Nitride nanoflakes for high-performance Na-ion Supercapacitors

Bhanu Ranjan[1] and Davinder Kaur[1]
[1]Functional Nanomaterials Research Laboratory (FNRL),
Department of Physics, Indian Institute of Technology Roorkee (IIT-Roorkee)
Roorkee-247667, Uttarakhand, India
branjan@ph.iitr.ac.in, davinder.kaur@ph.iitr.ac.in

**Abstract**

We report the fabrication of binder-free, low-cost, and efficient hybrid supercapacitive electrode based on the hexagonal phase of two-dimensional MoS$_2$ nanowires reinforced with molybdenum nitride nanoflakes deposited on stainless steel (SS) substrate using reactive magnetron sputtering technique. The MoS$_2$-Mo$_2$N/SS nanostructured thin film working electrode delivers a high gravimetric capacitance (351.62 F/g at 0.25 mA/cm$^2$) in 1M Na$_2$SO$_4$ aqueous electrolyte. The physisorption/intercalation of sodium (Na$^+$) ions in electroactive sites of MoS$_2$-Mo$_2$N nanocomposite ensures remarkable electrochemical performance. The deposited porous nanostructure with good electrical conductivity and better adhesion with the current collector demonstrates excellent capacitance retention of 93.62% over 4000 Galvanostatic Charge-Discharge (GCD) cycles. The attractive merits of the MoS$_2$-Mo$_2$N nanocomposite electrode make it a promising candidate for high-performance supercapacitor applications.

**Keywords:** MoS$_2$; Mo$_2$N; Supercapacitor; Sputtering; Binder-free; Synergistic Effect; High-Energy Density

**Introduction**

Over the last few years, Supercapacitors (SCs) have attracted significant recognition in the energy storage scientific community because of their numerous advantages, including high power density, high specific capacitance, excellent cyclability, low cost, and safe operation. However, their main downside is low energy density, which can be addressed by rationally designing hybrid materials.[1] The prime factor deciding the electrochemical performance of SCs is to design a specific electrode material and combine it with an appropriate electrolyte.[2] Recently, transition metal dichalcogenide (TMDs), especially MoS$_2$, has been explored in supercapacitors applications due to its rich intercalation chemistry, high surface area, and intrinsic high ionic conductivity.[3] Nevertheless, due to its inherently low electrical conductivity and poor cycling stability, MoS$_2$ alone may not be suitable as a highly-stable and long-lasting electrode material. Thus, composite-based electrodes of MoS$_2$ with highly conductive and stable materials are highly desirable.[4]–[6]

Molybdenum nitride, a transition metal nitride, is well recognized for its excellent electrical conductivity, superior cycling stability, and good resistance to electrochemical decomposition in an aqueous electrolyte.[7], [8] Therefore, we believe by introducing Mo$_2$N layers into the MoS$_2$ synthesis, a nanostructured composite material with much better electrochemical performance can be achieved. Owing to the multiple oxidation states (+2, +3, +4, +5, and +6) of Mo metal element, it acts as an excellent electroactive element in both MoS$_2$ and Mo$_2$N. It is also beneficial in boosting the pseudocapacitive charge storage mechanism. In the present work, we develop a hybrid electrode based on MoS$_2$-Mo$_2$N composite nanostructure sputtered directly onto the cost-effective stainless steel (SS) current collector. Reactive magnetron sputtering, a PVD technique, provides contamination and binder-free thin film synthesis, offers better adhesion, ensures good electrical conductivity, and is feasible for large-scale industrial fabrication.[9]–[13] Herein, the fabricated electrode delivers a very high gravimetric, areal, and volumetric capacitance in an aqueous electrolyte within a wide voltage window of 1.3V, suggesting its suitability for high-performance SCs electrodes. Compared with the individual electrodes, the hybrid demonstrates superior electrochemical performance, which is attributed to the synergistic effect between the layers of MoS$_2$ and Mo$_2$N.

**Experimental section**

Three different thin films, namely (a) $MoS_2$, (b) $Mo_2N$, and (c) $MoS_2$-$Mo_2N$ composite, were deposited onto polished SS substrates (2 cm × 1 cm) using reactive magnetron sputtering system (Fig. 1a,b). Firstly, polished SS substrates were placed inside the sputtering chamber at 6 cm distance from both the sputtering targets of Mo and $MoS_2$ (99.999% pure, Testbourne Ltd, UK). The turbomolecular pump backed by a rotary pump was used to evacuate the sputtering chamber up to a base pressure of $2\times10^{-6}$ Torr prior to the deposition. The targets were also pre-sputtered onto the shutter for 10 min to remove any contaminant layers. The $MoS_2$ thin film electrode is fabricated at 48 Watt DC power in a pure argon gas atmosphere and a constant deposition pressure of 10 mTorr. Instead, a DC power of 60 Watt in the presence of 90% (Ar) + 10% ($N_2$) gas mixture at 12 mTorr pressure is utilized for $Mo_2N$ layer deposition. Fig. 1a represents the schematic of the reactive sputtering chamber showing the deposition mechanism along with prepared thin film electrodes. The $MoS_2$-$Mo_2N$ composite electrode is prepared by the simultaneous sputtering of $Mo_2N$ and $MoS_2$ layers. A constant substrate temperature of 400º C is maintained throughout all depositions.
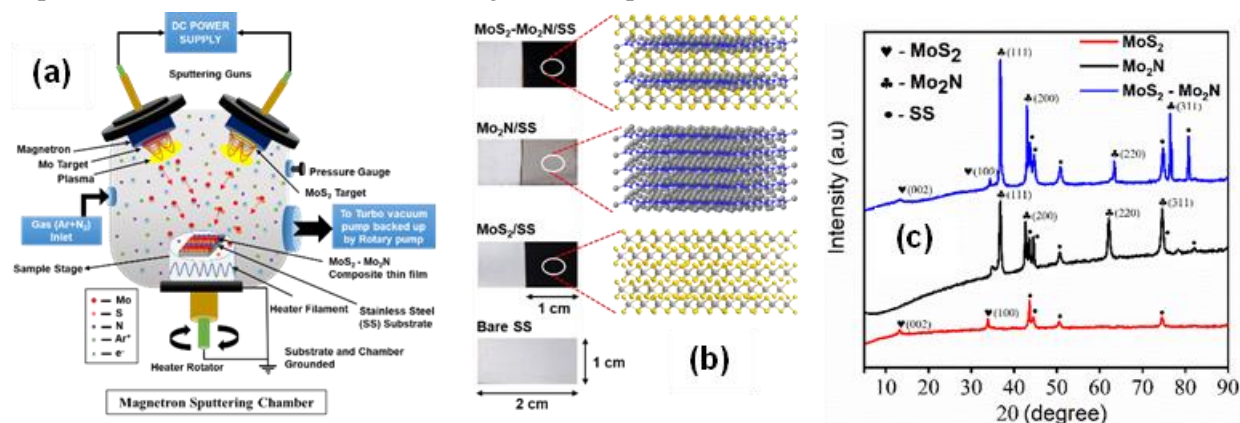


**Fig. 1. (a)** Schematic of the reactive magnetron sputtering system; **(b)** digital photograph and schematics illustrating the layered structure of fabricated thin film electrodes; and **(c)** XRD patterns of $MoS_2$, $Mo_2N$, and hybrid $MoS_2$-$Mo_2N$ thin films deposited on SS substrates.

**Results and Discussion**

The XRD patterns of the as-deposited thin film electrodes on SS substrates indicate their high crystallinity (Fig. 1c). It may be noted the peaks of SS appear in each diffraction pattern (marked with black dots). XRD peaks at 13.16° (002) and 33.71° (100) confirm the presence of hexagonal (2H) phase of $MoS_2$ (JCPDS no. 00- 37-1492).[4], [6], [14] The diffraction peaks at 37.4°, 43.5°, 63.1°, and 75.8° angles are indexed to (111), (200), (220) and (311) planes, respectively, of the γ-$Mo_2N$ (JCPDS no. 00-025-1366).[14] The FE-SEM surface and cross-sectional morphology of as-synthesized electrodes are presented in Fig. 2a-f. The FE-SEM images of $MoS_2$-$Mo_2N$ hybrid, pristine $MoS_2$, and $Mo_2N$ show three-dimensional (3D) nanostructures grown uniformly over the entire surface of the SS substrate. The $MoS_2$ and $Mo_2N$ samples show nanowires and nanoflakes-shaped morphology, respectively. On the other hand, the hybrid material indicates intermediate grain size with mixed nanostructures.

To probe into the electrochemical charge storage properties, the sputtered $MoS_2$, $Mo_2N$, and hybrid $MoS_2$-$Mo_2N$ electrodes are characterized in a three-electrode system immersed in 1M $Na_2SO_4$ electrolyte. The Cyclic Voltammetry (CV) profiles of the $MoS_2$-$Mo_2N$ hybrid at scan rates from 10 to 250 mV/s are displayed in Fig. 3a. At all scan rates, the curves exhibit a quasi-rectangular shape with weak redox peaks at -0.8 and -0.15 V, indicating pseudocapacitive behavior. Thereafter, the electrochemistry of pure $MoS_2$ and $Mo_2N$ electrodes at similar parameters is analyzed to compare with the hybrid electrode. As plotted in Fig. 4a, the gravimetric capacitance of the hybrid reduces from 235.04 to 145.51 F/g as the scan rate increase from 10 to 250 mV/s, which is superior to that of pristine $MoS_2$ and $Mo_2N$, respectively. Additionally, the hybrid electrode shows a

wide potential window (-1.0 to 0.3 V). Quantitively, the hybrid delivers a remarkably high areal and volumetric capacitance of 35.26 mF/cm$^2$ and 493.23 F/cm$^3$ at a sweep rate of 10 mV/s, respectively (Fig. 3b).
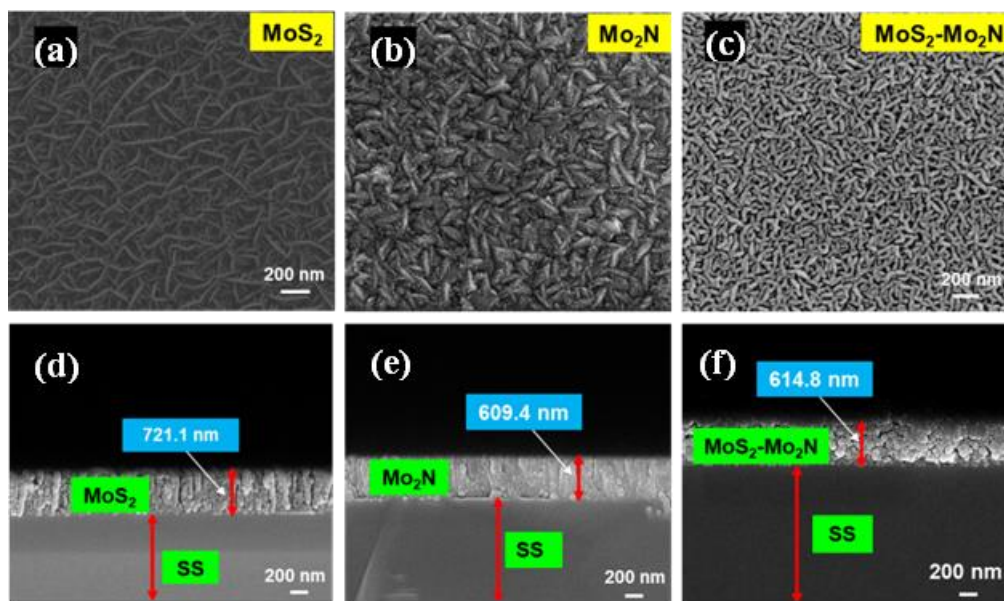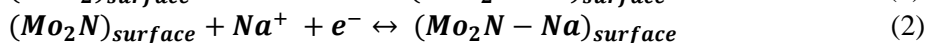


**Fig. 2.** FE-SEM surface morphology of; **(a)** MoS$_2$; **(b)** Mo$_2$N; and **(c)** MoS$_2$-Mo$_2$N samples grown on SS and cross-sectional FE-SEM images of; **(d)** MoS$_2$; **(e)** Mo$_2$N; and **(f)** MoS$_2$-Mo$_2$N samples.

**Table 1.** Various parameters for comparing the electrochemical performance of fabricated electrodes.

| Samples | $R_s$ ($\Omega$) | $R_{ct}$ ($\Omega$) | Potential Window (V) | Gravimetric Capacitance (F/g) |
|---|---|---|---|---|
| MoS$_2$ | 2.53 | 1.35 | 1.23 | 280.58 |
| Mo$_2$N | 4.68 | 1.78 | 1.4 | 250.80 |
| MoS$_2$-Mo$_2$N | 2.27 | 0.87 | 1.3 | 351.61 |

The physisorption of sodium (Na$^+$) ions can be explained by the following equation:

$$(MoS_2)_{surface} + Na^+ + e^- \leftrightarrow (MoS_2 - Na)_{surface} \tag{1}$$
$$(Mo_2N)_{surface} + Na^+ + e^- \leftrightarrow (Mo_2N - Na)_{surface} \tag{2}$$

The chemisorption or intercalation of sodium (Na$^+$) ions can be described by the following equation:

$$MoS_2 + Na^+ \leftrightarrow MoS_2 - Na^+ \tag{3}$$
$$Mo_2N + Na^+ \leftrightarrow Mo_2N - Na^+ \tag{4}$$

The specific capacitance for the hybrid electrode is calculated using Galvanostatic Charge-Discharge (GCD) cycles obtained at varying current densities (0.25, 0.50, 0.75, 1, 3, and 5 mA/cm$^2$) as depicted in Fig. 3c-d. The GCD curve shows an almost triangular shape with excellent coulombic efficiency. The existence of quasi-triangular curves suggests the presence of EDLC together with a pseudocapacitive mechanism. Furthermore, the variation of current density from 0.25 to 5 mA results in the reduction of areal capacitance from 52.74 to 16.36 mF/cm$^2$, and volumetric capacitance reduces to 228.88 from 737.86 F/cm$^3$ (Fig. 3d). The hybrid electrode delivers higher capacitance values than those of pristine MoS$_2$ and pure Mo$_2$N (Fig. 4b). In the variation of coulombic efficiencies as a function of current density shown in Fig. 4c, the hybrid electrode showed a reasonably high coulombic efficiency of 98.3 % at 0.25 mA/cm$^2$, which slightly drops to 93.24% at 5 mA/cm$^2$, manifesting fast charge-discharge and outstanding reversible kinetics. The fitted Nyquist plot, along with the equivalent circuit model of the hybrid electrode, is shown in Fig. 3e. The low value of $R_s$ (2.27 $\Omega$) and $R_{ct}$ (0.87 $\Omega$) suggests fast adsorption of Na$^+$ ions along with rapid redox kinetics. Also, the higher vertical inclination of the curve with the imaginary axis confirms its dominating capacitive nature (Table 3). To test the long-term cycling performance of hybrid electrode, a series of 4000 galvanostatic charge-discharge (GCD) cycles is performed at 2 mA/cm$^2$ current density (Fig. 3f). Excellent capacitance retention of 93.62% is maintained even after 4000 GCD cycles, indicating outstanding cycling stability of the MoS$_2$-Mo$_2$N hybrid electrode. The GCD

profiles corresponding to the first and last 10 cycles elucidate no appreciable change in their quasi-triangular shape.
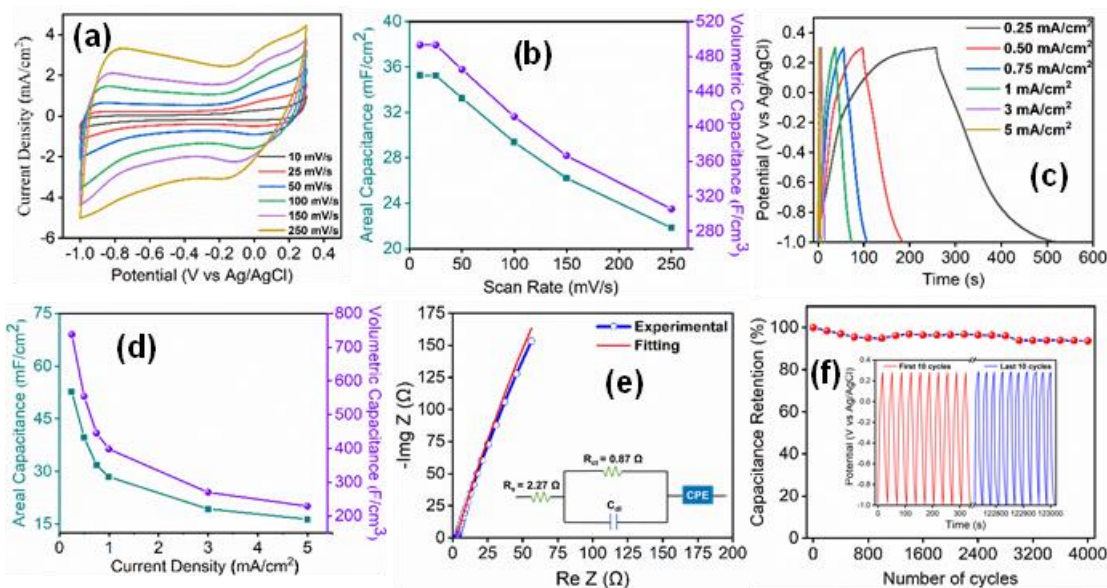


**Fig. 3.** Electrochemical performance of $MoS_2$-$Mo_2N$ hybrid electrode; **(a)** CV curves at scan rates from 10 to 250 mV/s and **(b)** evaluated areal and volumetric capacitances; **(c)** GCD curves at different current densities from 0.25 mA/cm² to 5 A/cm² and **(d)** evaluated areal and volumetric capacitances **(e)** Nyquist plot with fitted data (inset shows fitted equivalent circuit model) **(f)** GCD cycling stability test at 2 mA/cm² over 4000 GCD.
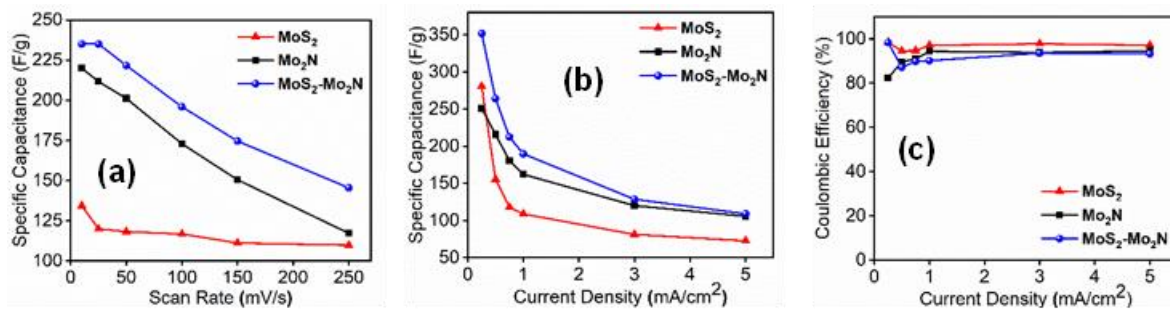


**Fig. 4.** Comparison of electrochemical performance of pristine $MoS_2$ and $Mo_2N$ electrodes with hybrid $MoS_2$-$Mo_2N$ electrodes; **(a)** specific capacitances at different scan rates from 10 to 250 mV/s; **(b)** at current density range from 0.25 - 5 mA/cm²; **(c)** coulombic efficiency measured at current density range in 0.25 to 5 mA/cm².

**Conclusion**

In summary, we have systematically employed the sputtering technique to investigate the coupling effect of molybdenum nitride into the $MoS_2$ nanowires. The fabricated electrode renders an excellent conductive pathway for charge carriers and eases $Na^+$ ion insertion/desertion. Electrochemical studies demonstrate the as-deposited $MoS_2$-$Mo_2N$ hybrid electrode at 400º C delivers a high gravimetric capacitance of 351.62 F/g, areal capacitance of 52.74 mF/cm², and volumetric capacitance of 737.86 F/cm³ at a current density of 0.25 mA/cm². In addition, the nanocomposite $MoS_2$-$Mo_2N$ electrode also reveals a large operating potential window of 1.3 V, making it a potential candidate for energy storage device applications. The hybrid exhibits superior electrochemically rich performance compared to the pristine $MoS_2$ and $Mo_2N$, owing to the synergistic integration of EDLCs and pseudocapacitive characteristics of the constituent layers.

**Acknowledgments**

**References**

1. Y. Wang, Y. Song, and Y. Xia, "Electrochemical capacitors: Mechanism, materials, systems, characterization and applications," Chem. Soc. Rev., vol. 45, no. 21, pp. 5925–5950, 2016, doi: 10.1039/c5cs00580a.
2. F. Wang et al., "Latest advances in supercapacitors: From new electrode materials to novel device designs," Chemical Society Reviews, vol. 46, no. 22. pp. 6816–6854, 2017, doi: 10.1039/c7cs00205j.
3. K. S. Kumar, N. Choudhary, Y. Jung, and J. Thomas, "Recent Advances in Two-Dimensional Nanomaterials for Supercapacitor Electrode Applications," ACS Energy Lett., vol. 3, no. 2, pp. 482–495, 2018, doi: 10.1021/acsenergylett.7b01169.
4. G. K. Sharma, B. Ranjan, and D. Kaur, "Two-dimensional $MoS_2$ reinforced with $Cu_3N$ nanoflakes prepared via binder less sputtering route for flexible supercapacitor electrodes," Appl. Phys. Lett., vol. 118, no. 20, p. 203901, 2021, doi: 10.1063/5.0045378.
5. N. Joseph, P. M. Shafi, and A. C. Bose, "Recent Advances in $2D-MoS_2$ and its Composite Nanostructures for Supercapacitor Electrode Application," Energy and Fuels, vol. 34, no. 6, pp. 6558–6597, 2020, doi: 10.1021/acs.energyfuels.0c00430.
6. B. Ranjan, G. K. Sharma, and D. Kaur, "Tuning growth of $MoS_2$ nanowires over NiTiCu nanostructured array for flexible supercapacitive electrodes with enhanced Li-ion storage," Appl. Phys. Lett., vol. 118, no. 22, p. 223902, 2021, doi: 10.1063/5.0048272.
7. M. S. Balogun, Y. Huang, W. Qiu, H. Yang, H. Ji, and Y. Tong, "Updates on the development of nanostructured transition metal nitrides for electrochemical energy storage and water splitting," Mater. Today, vol. 20, no. 8, pp. 425–451, 2017, doi: 10.1016/j.mattod.2017.03.019.
8. B. Ranjan, G. K. Sharma, and D. Kaur, "Rationally synthesized $Mo_2N$ nanopyramids for high-performance flexible supercapacitive electrodes with deep insight into the Na-ion storage mechanism," Appl. Surf. Sci., vol. 588, no. March, p. 152925, 2022, doi: 10.1016/j.apsusc.2022.152925.
9. G. K. Sharma, B. Ranjan, and D. Kaur, "Estimating Li-ion storage in semiconducting nanocomposite of $2D-MoS_2$ decorated aluminum nitride nanoflowers for flexible electrodes of supercapacitors," Appl. Phys. Lett., vol. 121, no. 1, 2022, doi: 10.1063/5.0093681.
10. G. K. Sharma, B. Ranjan, and D. Kaur, "Electrochemical kinetics of $2D-MoS_2$ sputtered over stainless-steel mesh: Insights into the Na+ ions storage for flexible supercapacitors," Ceram. Int., vol. 48, no. 16, pp. 23404–23414, 2022, doi: 10.1016/j.ceramint.2022.04.332.
11. B. Ranjan and D. Kaur, "Achieving enhanced pseudocapacitance in $MoS_2$ nanowires rationally sputtered over NiMnIn shape memory alloy for flexible Na-ion supercapacitor," J. Energy Storage, vol. 71, no. May, p. 108122, 2023, doi: 10.1016/j.est.2023.108122.
12. K. Kaushlendra, P. Kumar, D. Arora, B. Ranjan, and D. Kaur, "Remotely tuned multistate resistive switching in $MoS_2$/NiMnIn thin film heterostructure for highly flexible ReRAM application," Ceram. Int., no. September, 2022, doi: 10.1016/j.ceramint.2022.11.122.
13. B. Ranjan, G. Kumar Sharma, G. Malik, A. Kumar, and D. Kaur, "In-situ sputtered $2D-MoS_2$ nanoworms reinforced with molybdenum nitride towards enhanced Na-ion based supercapacitive electrodes," Nanotechnology, vol. 32, no. 45, 2021, doi: 10.1088/1361-6528/ac1bdf.
14. C. Huang et al., "Vertical kinetically oriented $MoS_2$-$Mo_2N$ heterostructures on carbon cloth: A highly efficient hydrogen evolution electrocatalyst," Sustain. Energy Fuels, vol. 4, no. 5, pp. 2201–2207, 2020, doi: 10.1039/d0se00144a.